Improving full-field identification using progressive model enrichments

Jan Neggers, Florent Mathieu, François Hild, Stéphane Roux, Nicolas Swiergiel

Improving full-field identification using progressive model enrichments

J. Neggers[a,*], F. Mathieu[a], F. Hild[a], S. Roux[a], N. Swiergiel[b]

[a] *LMT, ENS Paris-Saclay / CNRS / Université Paris-Saclay*
61 avenue du Président Wilson, 94235 Cachan Cedex, France
[b] *Airbus Group - Innovations, 12 rue Pasteur, 92152 Suresnes Cedex, France*

Abstract

Full-field identification methods such as finite element model updating or integrated digital image correlation minimize the gap between an experiment and a simulation by iterative schemes. Within the algorithms residual fields *and* sensitivity fields are used to achieve identification. This paper discusses how these same fields can be used to assess the quality of the identification and guide toward successive enrichment of the constitutive model to progressively reduce the experiment-model gap. A cyclic experiment on a dog-bone sample made of aluminum alloy is used as an example to identify the parameters of an elasto-plastic model with exponential hardening and anisotropic yielding.

Keywords: Anisotropic plasticity, Damage, Digital image correlation, Full-Field measurements, Identification

1. Introduction

There is a constant need for calibrating the parameters of material models. Most modern engineering materials are created from mixtures of multiple materials using highly specific micro-architectures [1]. This allows them to be optimized to a high extent. The interest in these materials is often beyond their linear elastic regime [2].

*Corresponding author
Email address: jan.neggers@ens-paris-saclay.fr (J. Neggers)

The mechanics of materials community has been prolific in providing an abundance of interesting nonlinear material models, each describing the material behavior with large sets of parameters [3]. At this moment, the experimental methods have reached a data density level rich enough to identify these multi-parameter nonlinear models. The main source for the increase in data density comes from the maturity of full-field measurement methods such as Digital Image Correlation (DIC [4, 5]).

The classical approach to parameter calibration is to optimize the experiment such that it is only sensitive to a limited number of material parameters [6]. For instance, uniaxial experiments gained popularity due to their near homogeneous stress state over the entire sample, which allow for estimations of stress and strain from the displacements and forces. Full-field methods enable one to deviate from this path since they capture the heterogeneous kinematics of the experiment [7, 8, 9]. In the latter each material point experiences a different stress/strain history and hence it may provide a different clue about the material model during a single experiment.

The most common identification method is referred to as Finite Element Model Updating (FEMU [10, 11, 12, 13, 14, 15]). In FEMU the gap between the experiment and simulations of the same experiment is minimized by optimizing (i.e. updating) the unknown model parameters. Within this paper a similar method is applied, which is referred to as Integrated-DIC [16, 17, 18, 19, 20, 21]. The latter optimizes the gap between simulation and experiment directly on the captured images by integrating the identification step in the DIC algorithm. However, the differences between the two methods are not essential for the discussion in this paper. The interested reader is referred to Ref. [20] for more details on this last point.

Full-field identification methods such as FEMU and Integrated-DIC use the gap between the experiment and simulations with different metrics, which can be made totally consistent [20]. This gap, or residual, is not only required inside the respective algorithms, it also provides means for visualizing where it is the largest in space and time. In this paper the residuals will be used

to progressively enrich the material model, thereby reducing the gap and thus improve the identification quality.

The full-field identification methods typically rely on sensitivity fields as part of the tangent operator in the iterative optimization algorithm [22, 23, 24]. As the name suggests they indicate the sensitivity of a certain parameter on space and time data of interest. Conversely, they show how the simulation will change with a small variation in a given parameter. In this paper it will be shown that these fields are invaluable to diagnose which part of the model is missing or wrong. The comparison between the sensitivity fields and the residual fields provides guidance on how to enrich the model and reduce their level.

Besides FEMU and Integrated-DIC there are other inverse identification methods (see e.g. [13] for an overview). This article focuses on two of these methods because both utilize the sensitivity fields in the same way. However, the concepts discussed herein may be equally valid for other identification methods such as the equilibrium gap method [25] or the virtual fields method [26, 27]. It is always possible to perform a simulation of the experiment with the obtained parameters of any identification method and compute the residual between the experiment and the simulation. These residuals are an accessible (though often omitted) tool for analyzing the quality of identification.

In Section 2, Integrated-DIC is briefly detailed in order to introduce concepts such as sensitivity fields and residual fields. Additionally, the tensile experiment on a dog-bone sample made of aluminum alloy 2219 is introduced and the finite element simulations are described. Section 3 discusses five identification cases using various constitutive models to analyze how successive enrichments can be used to assess identification quality. The five cases are discussed in parallel such that the differences between each can be discussed side-by-side. This parallel structure is beneficial for the discussion of the results. However, it is less optimal when introducing the five cases, which are inspired from each other based on results that will only be presented later on.

2. Identification Framework

The chosen identification method is Integrated-DIC (I-DIC). It integrates identification in digital image correlation by choosing the static and kinematic basis functions such that the degrees of freedom are directly the to-be-identified parameters. The interested reader is referred to the literature for additional details [28, 18, 20, 21]. However, the method is summarized to define certain aspects used to analyze the identification results. A related method is FEMU. In this method the distance between simulated and measured quantities, such as displacement [24] and/or force [10, 24], are minimized by iteratively updating the finite element model parameters. The key difference between FEMU and I-DIC is that FEMU minimizes the gap based on a measured displacement field and I-DIC minimizes the image residual directly using the model to drive the kinematics. This integration has advantages for cases where a fine mesh is required to accurately capture for instance complex sample geometry [17] or strain concentrations [29]. The displacement uncertainty of non-integrated DIC is inversely related to the element (or subset) size [30], where for I-DIC this is not the case since the degrees of freedom are not the nodal or subset displacements but the unknown material parameters. For cases where the smallest element size is not critical for DIC it can be shown that the two methods are equivalent, provided that the noise level is small and an appropriate metric is chosen in FEMU [20, 31].

2.1. Integrated DIC

In Integrated-DIC the objective is to seek the optimum set of parameters $\{p\} = \{p_1, \ldots, p_n\}$ that minimize the distance between a reference image f and a series of deformed images g_τ for a given region of interest and a series of time steps τ. The deformed images are back transformed using a displacement field u_τ that depends on the defined parameter set $\{p\}$. The objective is to minimize

the cost function,

$$\eta_I^2(\{p\}) = \frac{1}{2N_\tau N_k \gamma_I^2} \sum_\tau^{N_\tau} \sum_k^{N_k} \Big(f_k - \tilde{g}_{k\tau}(\{p\}) \Big)^2, \tag{1}$$

where, f_k denotes the gray value of a pixel at location x_k in the image of f and $\tilde{g}_{k\tau} = g_\tau\big(\underline{x}_k + \underline{u}_k(\{p\}, \tau)\big)$ denotes the corresponding interpolated gray values at the deformed locations in the image g for each time step τ. The number of pixels within the region of interest is N_k and the number of time steps is N_τ. The cost function is scaled with the gray level standard uncertainty of the image sensor γ_I and the number of measurements such that the expectation value of this cost function approaches unity when converged if only random acquisition noise were present.

For the experiments discussed within this paper, the force on the grips of the tensile machine was also captured during the experiments. To include these data in the identification method a second cost function is defined,

$$\eta_F^2(\{p\}) = \frac{1}{N_\tau \gamma_F^2} \sum_\tau^{N_\tau} \Big(F_\tau^{\exp} - F_\tau(\{p\}) \Big)^2, \tag{2}$$

where, $F_\tau^{\exp}$ is the measured force for time step τ and F_τ the corresponding simulated force. Again, this cost function is scaled with the standard uncertainty of the force sensor γ_F such that its expectation value approaches unity when converged in the presence of only acquisition noise.

Since the identified parameters must hold for both cost functions, they are combined to a single cost function,

$$\eta^2 = \frac{N_k}{N_k + 1} \eta_I^2 + \frac{1}{N_k + 1} \eta_F^2. \tag{3}$$

This extensive addition of the two cost functions is interesting as it provides the optimal cost function for the parameters in the sense that the resulting estimate will have the smallest variance provided the solution has converged and that the only uncertainty is acquisition noise.

The cost function (3) is minimized using Gauss-Newton's iterative routine that starts with an initial guess for $\{p_0\}$ and computes the iterative updates at

iteration l to the degrees of freedom $\{p\}^{(l+1)} = \{p\}^l + \{\delta p\}$,

$$[M]\{\delta p\} = \{b\}, \tag{4}$$

$$\big([M_I] + [M_F]\big)\{\delta p\} = \{b_I\} + \{b_F\}, \tag{5}$$

where, $[M]$ is the Hessian matrix and $\{b\}$ the right hand member. Typically, they are decomposed their respective counter parts for each individual cost function, namely, $[M_I]$, $[M_F]$, $\{b_I\}$ and $\{b_F\}$. They are defined as (for details see [20, 21]),

$$M_{Iij} = \frac{1}{2N_\tau N_k \gamma_I^2} \sum_\tau^{N_\tau} \sum_k^{N_k} \underline{\varphi}_{Ik\tau i} \cdot \underline{\nabla} f_k \, \underline{\nabla} f_k \cdot \underline{\varphi}_{Ik\tau j}, \tag{6}$$

$$b_{Ii} = \frac{1}{2N_\tau N_k \gamma_I^2} \sum_\tau^{N_\tau} \sum_k^{N_k} \underline{\varphi}_{Ik\tau i} \cdot \underline{\nabla} f_k \, \Big(f_k - \tilde{g}_{k\tau}(\{p\}) \Big), \tag{7}$$

$$M_{Fij} = \frac{1}{N_\tau \gamma_F^2} \sum_\tau^{N_\tau} S_{F\tau i} \, S_{F\tau j}, \tag{8}$$

$$b_{Fi} = \frac{1}{N_\tau \gamma_F^2} \sum_\tau^{N_\tau} S_{F\tau i} \Big(F_\tau^{\exp} - F_\tau(\{p\}) \Big), \tag{9}$$

where, $\underline{\nabla} f$ is the image gradient and $[\varphi_I]$ and $[S_F]$ are projection matrices that project the data space onto the parameter space. The image projection matrix is decomposed again using the FE shape-functions,

$$\underline{\varphi}_{Ik\tau i} = \frac{\partial \underline{u}_{k\tau}}{\partial p_i} \approx \sum_j^{N_a} \frac{\partial \underline{u}_{k\tau}}{\partial \underline{a}_{j\tau}} \frac{\partial \underline{a}_{j\tau}}{\partial p_i} = \sum_j^{N_a} \underline{\psi}_{kj\tau} \underline{S}_{Ij\tau i}, \tag{10}$$

where $\{\underline{a}\}$ are the nodal degrees of freedom of the FE mesh, N_a the number of degrees of freedom and $[\underline{\psi}]$ the corresponding FE shape-functions. The decomposition of $[\underline{\varphi}_I]$ into FE shape-functions and the image sensitivity matrix $[\underline{S}_I]$ is a common choice [19, 20]. It allows the shape-functions to be reused, which are also applied in a non-integrated DIC procedure and in the FE simulations that are run during the identification process. The image and force sensitivity matrices are then computed using finite differences,

$$\underline{S}_{Iij\tau} \approx \frac{\hat{\underline{a}}_{ij\tau} - \underline{a}_{j\tau}}{\epsilon p_i}, \tag{11}$$

$$S_{Fi\tau} \approx \frac{\hat{F}_{i\tau} - F_\tau}{\epsilon p_i}, \tag{12}$$

where $\{\underline{a}\}$ and $\{F\}$ are the respective nodal displacements and boundary forces for the current set of parameters while $\{\underline{\hat{a}}\}_i$ and $\{\hat{F}\}_i$ are the corresponding values for a calculation with one of the parameters p_i perturbed with a small factor, $\hat{p}_i = p_i + \epsilon p_i$. For all the results reported in this paper the perturbation factor is set to $\epsilon = 0.01$.

The sensitivity matrices presented in Equations (11) and (12) naturally follow from the derivation of Newton methods, and are a requirement for the optimization algorithm. However, they are also invaluable for analyzing sensitivities. They visually indicate where in space and time the experiment is sensitive to certain parameters, and will be shown and discussed later on. Because they can be computed before performing an experiment, they can be used to optimize the experiment [32, 33].

In the case of insignificant or limited sensitivity, Equation (4) is ill-conditioned. This difficulty is circumvented by using a Tikhonov-type regularization [34, 35], where the linear system of equations is modified to,

$$\Big([M] + \alpha[I]\Big)\{\delta p\} = \{b\} + \alpha\big(\{p_{\text{ref}} - \{p\}\}\big), \tag{13}$$

where, $\{p_{\text{ref}}\}$ is a set of reference parameters obtained from other sources such as other experiments and or expert knowledge. $[I]$ is the unity matrix and α the regularization strength, which is set to $10^{-5}\lambda$, where λ is the largest eigenvalue of $[M]$. The consequence of this regularization is that insensitive parameters will tend to the reference levels instead of the otherwise erratic identification behavior. The chosen α parameter is set sufficiently small such that parameters with reasonable sensitivity are determined by the Integrated-DIC procedure based on the experimental data. It is always possible to set $\alpha = 0$ and return to the original un-regularized system to analyze the influence of this regularization.

The remaining ingredients in this identification algorithm are the boundary conditions that are applied to the simulations, both when computing the image residual in Equation (7) and when computing the sensitivity matrices (Equations (11)-(12)). There are different options each with their own merits. For the cases discussed in this paper a method was adopted that applies the dis-

placement boundary conditions measured by a non-integrated FE-based DIC methods that uses the same mesh. This has the advantage of instantaneously aligning and synchronizing the measured and simulated data sets. Additionally, this method limits the simulation domain to the part that is visible within the field of view thereby reducing some computational costs. It has the disadvantage that these measured boundary conditions contain measurement uncertainty that is directly transferred to the identification algorithm.

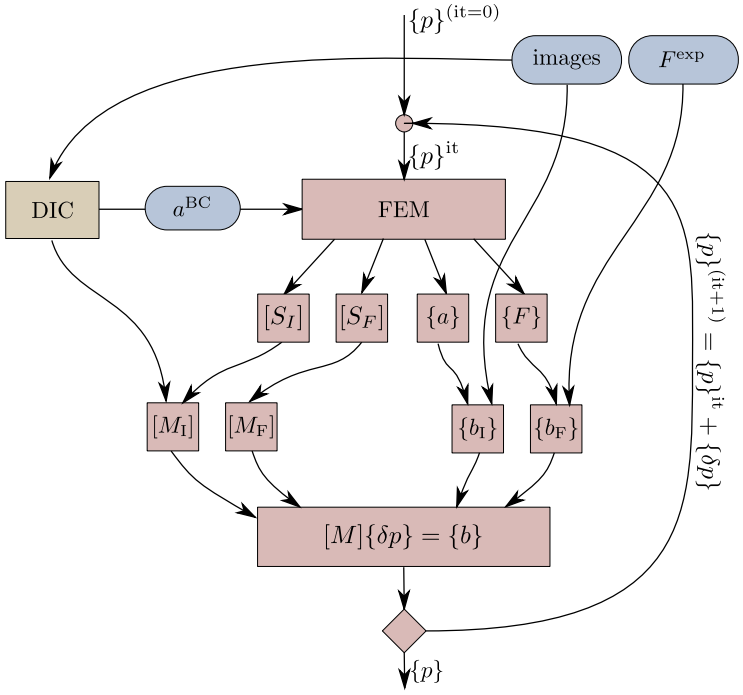

Figure 1: Integrated-DIC represented as a flow-chart. All blue items (with the rounded corners) are constants and are only computed before identification. The red items constitute the Integrated-DIC routine

Figure 1 shows the most important ingredients of the Integrated-DIC routine. To summarize, the method starts with a regular DIC routine to measure the boundary conditions a^{BC}, which together with an initial guess of the parameters, are the inputs to the FE simulations. From the simulations the sensitivity fields and the simulated versions of the measurement data are computed. All

measured and simulated data concentrate in Equation (4) where a single system of equations is formulated. The solution to this small system of equations is trivial and provides the update to the unknowns, which are the material parameters. The process is repeated until convergence which for the discussed cases is reached when the relative update norm is less than 10^{-3}.

2.2. Experiment

The example experiment chosen as the integral part of the discussion is a relatively simple dog-bone sample made of AA2219 as shown in Figure 2(a). The presented Integrated-DIC method can easily handle more complex geometries and inhomogeneous stress states [17, 29]. However, discussion of the gap between identification and measurement is equally important for classical identification methods. For that reason, a case was chosen that may seem trivial but, as will be discussed throughout the paper, contains nontrivial aspects.

The sample is 2 mm thick and 100 mm long, the width at the narrowest section is 10 mm, with the dog-bone radius of each side of the sample equal to 120 mm. The sample is loaded in a servo-hydraulic tension/compression testing machine equipped with a 50 kN load-cell. The top grip of the tensile machine is stationary while the bottom grip is driven at constant velocity of 0.01 mm/s to specific load levels (i.e. [1.8, 6.0, 8.5, 9.1, 9.3, 9.5, 9.6] kN). When a specific load level is reached the sample is unloaded to 0.1 kN upon which the next load cycle starts. At the end of the 7^{th} cycle the sample has not failed yet. Failure will occur in the 10^{th} cycle, at a failure strain of approximately 8% and a maximum load of 9.7 kN. In the last three cycles, localization starts to set in, resulting in a behavior that is too challenging for the applied constitutive models. The application of more sophisticated models is possible and interesting but considered beyond the scope of this paper.

A single Manta G-223 camera equipped with a telecentric lens of magnification $\times 0.125$ captured one side of the speckle-painted sample at 5 second intervals. This acquisition rate resulted in 152 images of which the first is in the unloaded configuration resulting in 151 loaded time steps up to the maximum

load of the 7^{th} cycle. The recorded images are of size 1120 $\times$ 2160 px, where each pixel captures the intensity of 26 $\times$ 26 µm^2 of the sample area digitized with 16 bits. The dynamic range, which is defined as the difference between the brightest and the darkest pixel, is 63,589 gray levels.

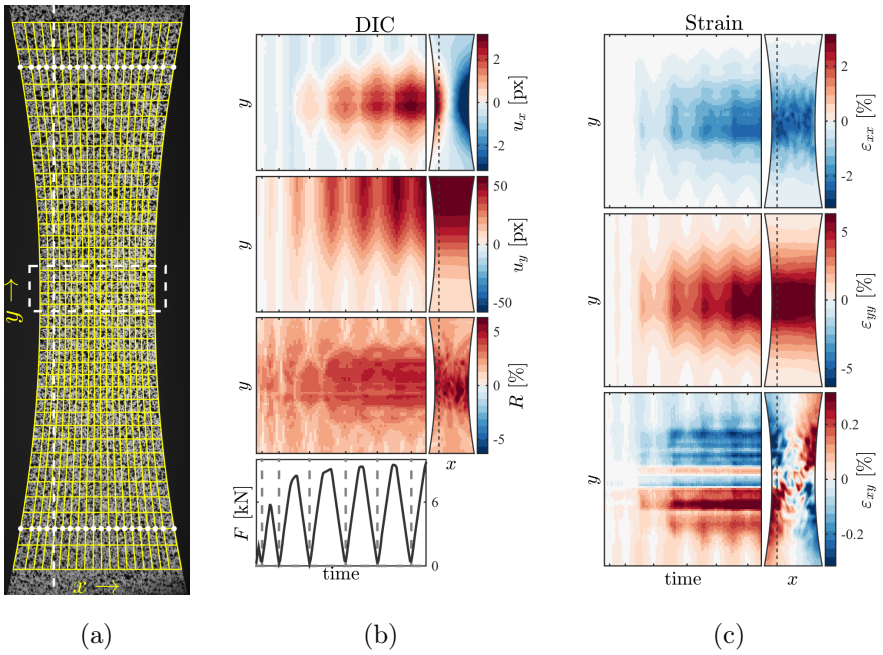

Figure 2: (a) Reference image f and mesh applied for both DIC and I-DIC purposes. (b) Measured displacement field obtained by DIC per component (i.e. $\underline{u} = u_x\underline{e}_x + u_y\underline{e}_y$) is shown for the last time step (right) and for one cross-section along time (left), the cross-section location is indicated with the dashed line (x = 165 px). The measured force is also shown below the displacement field. (c) Corresponding strain field using the same space and time visualization layout

The sample deformation that occurred during the experiment is summarized in Figure 2(b) showing the displacement and Figure 2(c) shows the logarithmic strain. A small explanation on the graphical layout of these figures may be required. It is a challenge to efficiently format the figures for print such that the most important information is available at the smallest expense of page real-estate. Therefore, a specific space-time layout is designed, which will be

used consistently throughout the paper. For each vector or tensor component, the full-field results are shown for the final time step (on the right), while the space-time results are shown for one column of pixels, i.e. $x = 165$ px (on the left). Whenever required the corresponding measured force/time plot is drawn below, sharing the same time abscissa as the space-time figures.

2.3. Measurement Uncertainty

Besides the 152 image captured during the experiment an additional 20 images were acquired before the experiment. During this capture the sample was mounted in the tensile testing machine that controlled the force level around zero. These 20 images should have zero displacement and zero force and thus allow for an assessment of the measurement uncertainty. From these images, the gray level uncertainty γ_I, the displacement uncertainty γ_U and the force uncertainty γ_F are estimated,

$$\begin{aligned} \gamma_I &\approx 652 \text{ GV}, \\ \gamma_U &\approx 0.017 \text{ px} \approx 0.44 \text{ µm}, \\ \gamma_F &\approx 5 \text{ N}. \end{aligned} \tag{14}$$

In the adopted Integrated-DIC algorithm only γ_I and γ_F are used to scale the cost functions. The application of γ_I assumes that the displacement uncertainty can be propagated using the DIC Hessian [30]. If this assumption is true, the following relation should hold,

$$\gamma_{a_i} = \frac{\gamma_I \sqrt{6}}{G L_i} \tag{15}$$

$$\hat{\gamma}_U = \langle \gamma_a \rangle \approx 0.0058 \text{ px} \approx \frac{1}{3} \gamma_U, \tag{16}$$

where G is the mean field average of image gradient and L_i is the element length for each node i, which is estimated as the square root of the area of the connected elements. There is a factor of three between the measured displacement uncertainty and the theoretical displacement uncertainty. There can be a number of reasons for this, not limited to, cross-pixel correlation, speckle quality and degradation, and sub-pixel interpolation errors. To remedy this gap, an

effective gray level uncertainty is computed $\hat{\gamma}_I \approx 3\gamma_I = 1911$ gray values, which is that ultimately used in Equation (3).

2.4. Finite Element Simulations

The Integrated-DIC routine is part of the Correli 3.0 framework, which is in continuous development at LMT [36]. The Integrated-DIC implementation configures the FE simulations with the correct parameters and subsequently calls the commercial code Abaqus implicit[1] to perform the simulations. The latter ones return the displacement field and reaction forces to the I-DIC implementation, which uses these data to compute the residuals and sensitivity fields, and then prepares for the next identification iteration (see Figure 1).

Part of the simulations are the displacement boundary conditions on each end of the sample. The displacements measured by DIC of the 3$^{\text{rd}}$ row of nodes from each end inward are used, which are indicated with circular markers in Figure 2(a). The far edge nodes are not used because the images have a significant reduction in intensity due to vignetting at the top and bottom image edges. Moreover, the edge nodes of FE-based DIC routines are always more sensitive to noise due to their reduced connectivity [30]. To further reduce the impact of measurement noise in the simulations, the measured boundary conditions are smoothened using a cubic polynomial fit along the line of nodes for each time step.

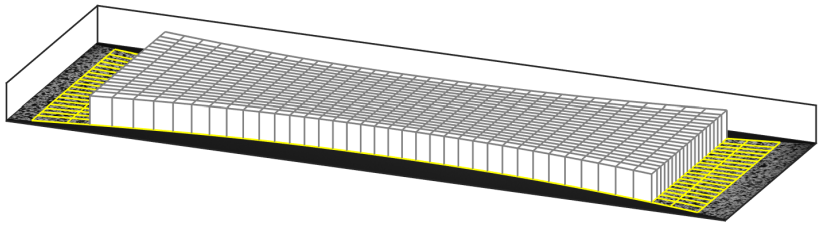

Figure 3: 2D mesh as used in the DIC analyses and 3D mesh as used in FE simulations

[1] Abaqus Standard: Dassault Systèmes Simulia [37]

The FE simulations are performed in 3D, using an extruded version of the DIC mesh as shown in Figure 3. The in-plane boundary conditions are applied identically to the front and the back sample surfaces. The out-of-plane boundary conditions are set to zero only for the front surface. Note that in the experiment the sample is clamped roughly 3 cm farther outward. The sample has an acceptable thickness to length ratio to be close to plane-stress. Therefore, it could be modeled in 2D instead of 3D. This hypothesis was tested and significant differences in the identified parameters between the 2D plane-stress and a 3D case were detected, especially for the Poisson's ratio. Modeling the sample with multiple elements over the thickness was also tested but proved not to significantly change the identification result while significantly increasing the computation time.

3. Identification Results

At the core of this paper is the discussion about the differences between identification cases and how the residuals of one case can guide choices made in the following one. In this section five cases are discussed, each extending on the previous one. Although the cases depend chronologically upon each other, they will be discussed in parallel such that the results can be compared side by side. Consequently, the five cases will be introduced in parallel without the support of their data, causing some choices to seem unsupported at first sight.

3.1. Identification Cases

The five identification cases are defined as in Table 1. The first two cases (i.e. C1 and C2) allow for a direct comparison between classical (e.g. a stress-strain fit) and full-field (e.g. I-DIC) identification approaches. The Cases C2 to C4 progressively include more material parameters, and thus more freedom for the optimization method to reduce the residuals. Case C5 reduces the number of degrees of freedom by removing the Voce part of the hardening model and

identifying only the Ludwik hardening model with Hill anisotropy. The following sections will discuss the details of the specific models.

Table 1: Definition of the five identification cases

	Identification method	Hardening model	Anisotropy	Number of parameters
C1)	Classical	Ludwik	-	5
C2)	I-DIC	Ludwik	-	5
C3)	I-DIC	Ludwik-Voce	-	7
C4)	I-DIC	Ludwik-Voce	Hill 48	10
C5)	I-DIC	Ludwik	Hill 48	8

3.2. Hardening Models

To showcase the method of successively enriching the identification algorithm a selection of hardening models is considered. There exist many interesting modern hardening models for sheet metals [38], most of which include anisotropy. However, for the present paper, basic models suffice with the added benefit of not complicating the discussion. As a preliminary study, the following five hardening models are discussed in Case C1,

$$\text{Elastic:} \quad \sigma = E\epsilon, \qquad \sigma \leq \sigma_0, \tag{17}$$

$$\text{Swift:} \quad \sigma = d(\epsilon_0 + \epsilon_p)^b, \qquad \sigma > \sigma_0, \tag{18}$$

$$\text{Ludwik:} \quad \sigma = \sigma_0 + h\epsilon_p^m, \qquad \sigma > \sigma_0, \tag{19}$$

$$\text{Voce:} \quad \sigma = \sigma_\infty - (\sigma_\infty - \sigma_0)\exp(-n\epsilon_p), \qquad \sigma > \sigma_0, \tag{20}$$

$$\text{Ludwik-Voce:} \quad \sigma = \sigma_0 + h\epsilon_p^m + (\sigma_\infty - \sigma_0)\exp(-n\epsilon_p), \qquad \sigma > \sigma_0, \tag{21}$$

where ϵ_p is the plastic strain in the load direction, E the Young's modulus, σ_0 the yield stress and ϵ_0, d, b, h, m, σ_∞ and n are the hardening parameters of the various models [39]. Not shown in the above equations is the Poisson's ratio ν adding another degree of freedom for identification.

3.3. Anisotropic Yielding

To enrich the material model with anisotropic plasticity, Hill's model is selected [40] since it is a readily available option in Abaqus [37]. The anisotropic

plasticity criterion used in Cases C4 and C5 is defined as

$$H_1(\sigma_{22}-\sigma_{33})^2 + H_2(\sigma_{33}-\sigma_{11})^2 + H_3(\sigma_{11}-\sigma_{22})^2 + 2H_4\sigma_{23}^2 + 2H_5\sigma_{31}^2 + 2H_6\sigma_{12}^2 = 1, \quad (22)$$

with

$$H_1 = \frac{1}{2}\left(\frac{1}{R_{22}^2} + \frac{1}{R_{33}^2} - \frac{1}{R_{11}^2}\right), \qquad H_4 = \frac{3}{2}\frac{1}{R_{23}^2}, \quad (23)$$

$$H_2 = \frac{1}{2}\left(\frac{1}{R_{33}^2} + \frac{1}{R_{11}^2} - \frac{1}{R_{22}^2}\right), \qquad H_5 = \frac{3}{2}\frac{1}{R_{13}^2}, \quad (24)$$

$$H_3 = \frac{1}{2}\left(\frac{1}{R_{11}^2} + \frac{1}{R_{22}^2} - \frac{1}{R_{33}^2}\right), \qquad H_6 = \frac{3}{2}\frac{1}{R_{12}^2}, \quad (25)$$

where R_{11}, R_{22}, R_{33}, R_{12}, R_{13} and R_{23} are yield stress ratios. For a plane-stress case, these ratios are interrelated such that four parameters suffice to fully describe the yield surface [38]. Therefore, for Cases C4 and C5 the parameters R_{22}, R_{33}, R_{12} and σ_0 are used adding 3 parameters to the identification routine.

3.4. Classical Identification

The classical way of identifying the material parameters is by fitting the hardening laws defined by Equations (18)-(21) on experimental stress/strain data. The stress and strain need to be derived from the measured data, which requires some assumptions. In this case, the application of DIC allows for a more local measurement of the strain, which is provided by averaging the strain fields shown in Figure 2(c) within a virtual strain gauge that encompasses the high strain area in the center of the sample (indicated by the dashed box in Figure 2(a)). If no local measurement is used, the strain in the sample has to be estimated from the elongation considering the geometry of the specimen. Knowing the strains more locally is an advantage when computing the stresses since it can be used to correct the cross-sectional area by assuming incompressibility

$$\sigma = \frac{F}{A} \approx \frac{F\exp(\epsilon)}{A_0}, \quad (26)$$

where σ is the yy-component of the true stress, A_0 and A the cross-sectional areas in the reference and deformed states, respectively. This estimation of the

stress in a uniaxial experiment is perhaps not the most sophisticated and may introduce some identification errors that may be prevented. However, for the studied experiment the maximum strain level was of the order of 7 % and thus Equation (26) is assumed to be reasonably accurate.

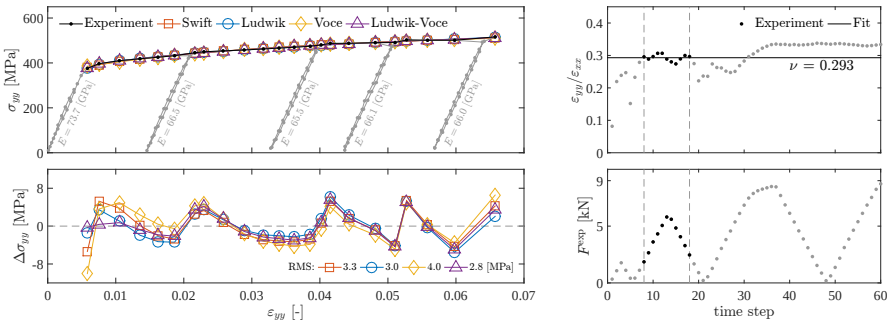

(a) (b)

Figure 4: (a) Stress/strain response as computed from the measured force/displacement, fitted with the hardening models defined in Equations (18)-(21) and the difference between the fitted and measured stress $\Delta\sigma_{yy}$. (b) The strain ratio obtained from the average strain inside the virtual strain gauge, the average ratio over the time interval marked by the vertical lines, is used to identify Poisson's ratio. The force/time plot shows that the chosen data points are those with significant force within the elastic regime of the experiment

Figure 4(a) shows that all 4 proposed hardening models can adequately describe the hardening behavior. The first three hardening models (i.e. Swift, Ludwik and Voce) each use three parameters, while the last (i.e. Ludwik-Voce) uses 5 parameters. Of the three parameter models, Ludwik's model has the lowest residual, while the Ludwik-Voce model improves the residual, most notably near the onset of plasticity. As a consequence, Ludwik's model and the Ludwik-Voce model will be studied further later on.

Figure 4(b) shows the strain ratio for the first few cycles. For time steps where the strain level is too small the ratio becomes highly sensitive to noise. Therefore, only the time steps for the second cycle are used to calibrate ν. The second cycle is assumed to be fully elastic, which is reinforced by the third cycle that shows yielding at a much higher force level. Additionally, it is possible to

measure the Lankford ratio from the ratio of the two strain components in the plane orthogonal to the loading direction,

$$r = \frac{\epsilon_{xx}}{\epsilon_{zz}} \approx 0.55, \tag{27}$$

where ϵ_{xx} is measured directly while ϵ_{zz} can be estimated supposing incompressibility. Assuming simple anisotropy, i.e. $R_{22} = 1$, allows for the determination of R_{33}

$$R_{33} = \frac{r(r+1)}{2r} \approx 0.89, \tag{28}$$

which shows that the material is plastically anisotropic as expected for rolled aluminum sheets. Obtaining R_{22} from single point measurements like strain gauges would require a second experiment where the material is tested at 90 ° with respect to the rolling direction. Similarly identifying R_{12} would require an experiment at 45 °. Full-field data may allow for identification of all three in-plane anisotropy parameters from a single experiment, which will be discussed next.

3.5. Sensitivity Fields

The sensitivity matrices as defined in Equations (11)-(12) can be visualized in the same space-time representation as used throughout the paper. In this visual form they are referred to as sensitivity fields, since they have a similar form as displacement fields. The five sensitivity fields shown in Figure 5 are used for identification purposes in Case C2.

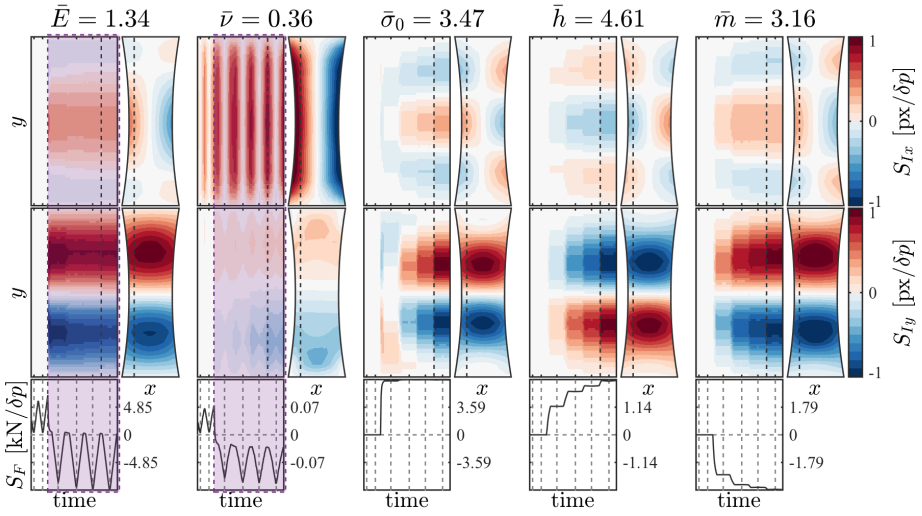

Figure 5: Sensitivity fields in terms of displacement S_I and force S_F for the five material parameters used in all five cases. Note that S_{Ix} and S_{Iy} fields are normalized to equalize their color ranges. Their respective amplitudes are given above the figure ($\bar{p}_i$). The purple dashed boxes in the sensitivity fields for E and ν indicate the zone where sensitivity is set to zero

Each sensitivity field has displacement parts S_{Ix}, S_{Iy} and force part S_F. Considering first the displacement parts, they are normalized to bring the fields in a single plottable color range. Due to this, the fields represent the sensitivity shape, while their amplitudes are written above the respective field ($\bar{p}_i$). These amplitudes underline the displacement sensitivity for each parameter. For example, for a 1 % change in Young's modulus, the change in displacement would be 0.013 px for the dark red areas and -0.013 px for the dark blue areas (i.e. at the extremes of the color bar). Assuming a 1 % change in each parameter, these values show that the first two parameters (i.e. E and ν) have a sensitivity below the displacement uncertainty ($\gamma_U = 0.017$ px), while the others (i.e. σ_0, h and m) are more sensitive than the uncertainty. The same analysis can be performed on the force side of the sensitivity analysis. All force sensitivity signals are higher than the expected force uncertainty, $\gamma_F = 5$ N, except for the Poisson's ratio, which is of the same order of magnitude.

For Case C3, two additional sensitivity fields are added to the identification routine, namely, those describing the exponential hardening (i.e. σ_∞ and n). Cases C4 and C5 consider anisotropic yielding, which adds another three parameters (i.e. R_{22}, R_{33} and R_{12}). The sensitivity fields corresponding to these five parameters are shown in Figure 6. Analyzing these sensitivity fields reveals that σ_∞ and R_{22} are very sensitive in force, but also in displacements, R_{33} has low force but significant displacement sensitivity, while n and R_{12} are neither sensitive in displacement nor in force. The low sensitivity of n and R_{12} (and also ν) will cause them to remain closer to their initial values as compared to the unregularized situation. This is a necessary drawback of using Tikhonov regularization without which the method is unstable and no solution is obtained.

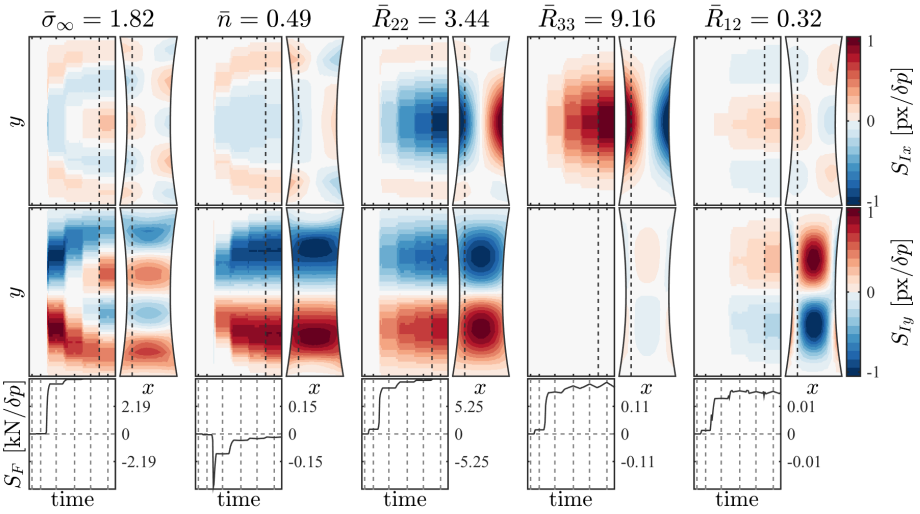

Figure 6: Sensitivity fields in terms of displacement S and force P for the five extra material parameters used in Case C4. The first three are also used in Case C3. Note that the S_x and S_y components are scaled with a normalization value shown above the figure ($\bar{p}_i$) to equalize the color ranges

Figure 4a shows the elastic modulus as fitted on each of the elastic unloading data. The moduli obtained on all but the initial elastic data are significantly lower than the initial modulus (i.e. 66 MPa vs. 73 MPa). Consequently, if the elastic parameters (i.e. E and ν) would be identified using the entire data

set, they would be sensitive to this stiffness reduction. Within the adopted Integrated-DIC method it is possible to counter this sensitivity by setting the sensitivity matrices $[S_I]$ and $[S_F]$ to zero for all time steps that occur after the onset of plasticity. In general this will result in a less optimal identification with higher residuals. However, the resulting identified elastic parameters would adhere more to how they are typically defined. Not limiting the elastic sensitivity to the initial regime would result in elastic parameters that are effective, or average, parameters. Ideally, the constitutive model should be enriched to include a mechanism such as damage that can account for this reduction in stiffness, but that is considered outside of the scope of this paper. For all full-field identification cases (i.e. C2-C5) the sensitivity fields for E and ν are set to zero after $\tau = 30$ as indicated with the dashed purple boxes in Figure 5.

3.6. Identified Parameters

The results from the five identification cases are summarized in Table 2. All four integrated methods converged in 10 iterations or less, which is mostly a consequence of the quality of the initial guess for which the obtained parameters from the previous case were used. All five methods returned comparable parameters, which gives confidence that their values are trustworthy. The identified elastic and plastic parameters are in line with typical values found in literature. Without further data, it is not possible to decide which identified parameters adhere more closely to the reality. However, the residuals, which will be discussed later on, decrease from Cases C1 to C5 showing that the last case more closely describes the experiment.

Table 2: Identified parameters for the five different identification cases

	E	ν	σ_0	h	m	σ_∞	n	R_{22}	R_{33}	R_{12}
	GPa	-	MPa	MPa	-	MPa	-	-	-	-
C1) Ludwik	73.7	0.29	363	588	0.48	-	-	-	-	-
C2) Ludwik	71.8	0.28	331	487	0.34	-	-	-	-	-
C3) Ludwik-Voce	72.5	0.29	284	502	0.21	242	393	-	-	-
C4) Ludwik-Voce-Hill	72.3	0.30	274	491	0.20	222	429	1.03	0.89	1.44
C5) Ludwik-Hill	71.7	0.30	372	561	0.35	-	-	0.91	0.86	1.33

The hardening parameters changed more significantly between the identifi-
335 cation cases. The low σ_0 values for C3 and C4 are the consequence of the exponential hardening law that significantly influences the early plasticity regime. It is important to note that, although the plastic parameters change, the corresponding stress/strain curves are nearly indistinguishable (see Figure 7).

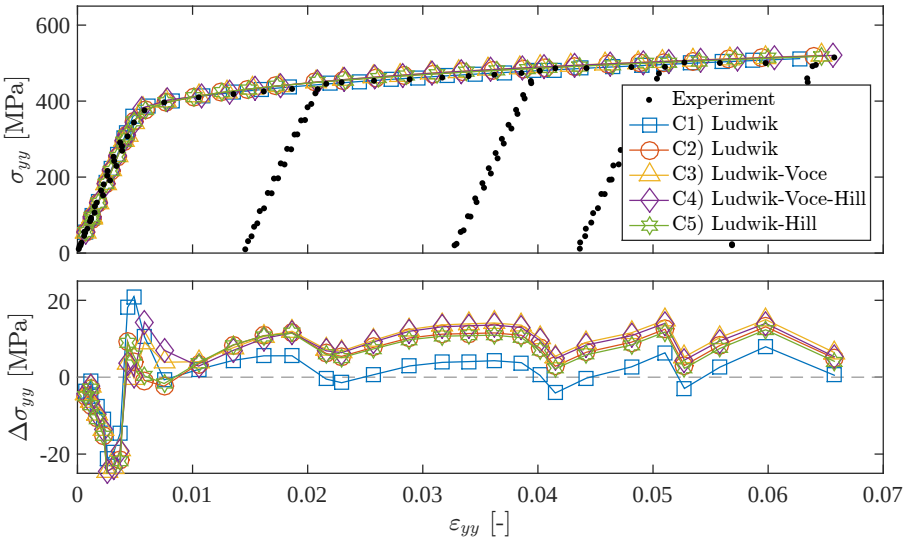

Figure 7: Stress/strain response for each case using the parameters listed in Table 2

All five parameter sets given in Table 2 are valid representations of the mate-
340 rial behavior and will provide predictive capabilities. Since the parameters are not strictly uncoupled, enriching the material description will inevitably lead

to a change in the previously identified parameters. Consider for instance the R_{22} parameter, which is strongly affected by the presence of the Voce model. Without further experiments it is difficult to definitely conclude that this stiffness reduction is due to damage or anisotropy. However, the lower residuals obtained for Case C4 (discussed in the next section) indicate that C4 is a more likely solution.

Last, it is emphasized that full-field identification methods are able to identify complex material models from such a simple experiment. The identification capacity would only increase for inhomogeneous experiments, enabling the identification of more complex and realistic models.

3.7. Residuals

This section discusses three types of residuals, namely, displacement, image and force residuals. It should be noted that only the last two are considered in I-DIC. The displacement residual is available because a non-integrated DIC analysis is also performed. Additionally, the analysis of these full-field residuals for classical identification methods is possible due to the availability of a simulation of the experiment using the obtained parameters.

Table 3 shows the global residuals for each identification case. The most significant residual is the 317 N level in force for Case C1. A second observation is that the total residuals η consistently decrease from one Case C1 to C4. This trend proves that each of these cases describes the experiment better than its predecessor.

Table 3: Residuals remaining after convergence for each of the five identification cases, η is the total residual of the cost function (Equation (3))

		R_U [px]	R_I [%]	R_F [N]	η [-]
C1)	Classical	0.28	4.94	317	1.66
C2)	Ludwik	0.26	4.71	197	1.58
C3)	Ludwik-Voce	0.26	4.69	217	1.57
C4)	Ludwik-Voce-Hill	0.13	3.3	214	1.11
C5)	Ludwik-Hill	0.14	3.37	197	1.13
	DIC	-	2.83	-	-

Figure 8 shows the full residuals for each case in space and time for the displacement, image, and force. They are a detailed representation of the distance between the experiment and its simulation. Full-field identification methods typically give access to these residuals. Classical identification cases rarely have access to these residuals, since they require simulating the experiment with the calibrated parameters, something that is typically not required for the identification [6]. However, it is in all cases possible to generate these residuals and use them to analyze where in space and time the identification was within the expected accuracy.

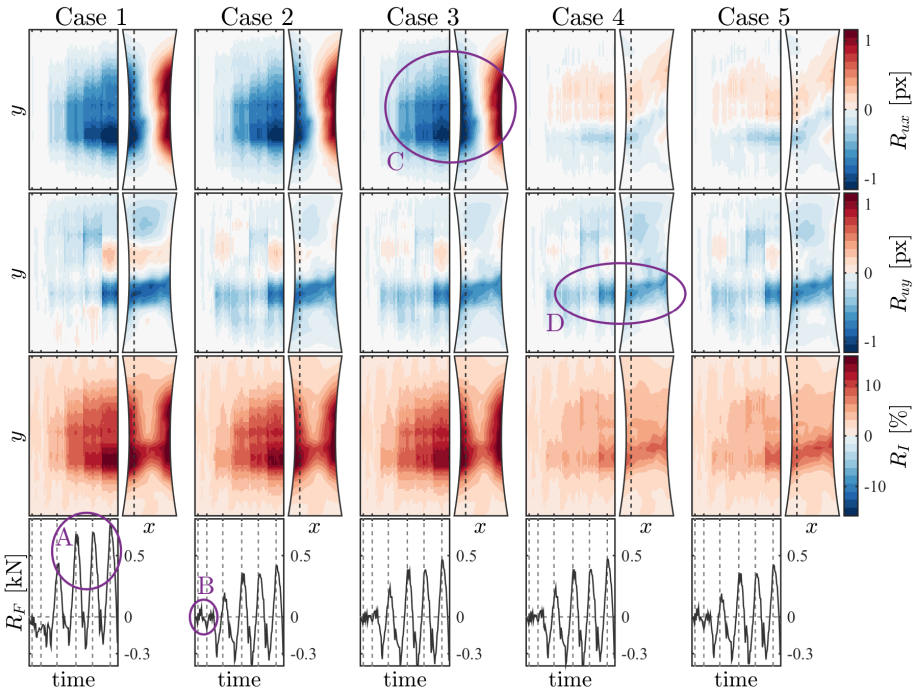

Figure 8: Full-field residuals for all five cases (Table 1). The top two rows show the displacement residuals as compared to DIC, the third row shows the image residuals and the bottom row shows the force residuals. The ellipses marked A to D are discussed in the text

Case C1 shows the residual fields as obtained by using the parameters from classical identification. Although, this identification method has the lowest residuals in terms of stress-strain (Figure 7), it has the highest image and force residuals. Whether these residuals are acceptable depends on the application of the identified model. In any way, they are much larger than the expected measurement uncertainty. Moreover, they are non-white, they have a structure or signature indicating that the gap between the model and the experiment is due to the limitations of the applied model.

Case C2 is the full-field version of Case C1, calibrating the same model parameters. The minimization on the image and force residuals will naturally reduce them. For this case the most significant reduction comes from the force

residual (see the ellipse marked A in Figure 8). The absence of significant reductions in the image and displacement residuals indicates these residuals are not due to identification errors but are the consequences of limitations of the chosen constitutive model.

Case C3 is the enriched version of Case C2 by adding an exponential part to the hardening law. The additional three degrees of freedom did not significantly improve the residuals. There is a minor signature in the early plasticity regime (see the ellipse marked B in Figure 8). From these residuals it is clear that both versions of the hardening law perform comparably but do not resolve the most significant remaining residual.

Case C4 adds anisotropy to the identification. It significantly improves the full-field residuals. A signature in the x-component of displacement R_{ux} is strongly reduced while also reducing a large portion of the image residual (see the ellipse marked C in Figure 8). It is interesting to note that the shape of the removed residual resembles the sensitivity field of R_{22} and R_{33} shown in Figure 6.

Case C5 removes the exponential hardening degrees of freedom that were added in Case C3 while retaining the anisotropy degrees of freedom. Similarly to the comparison of C2 and C3, in comparison between C4 and C4 the differences are limited. There is a zone in the R_{uy} residual that is similar in signature but less pronounced in Case C4 and the same force residual signature has returned in the early plasticity regime (see the ellipses marked D and B in Figure 8 respectively).

Ultimately, the case with the lowest residuals is Case 4. This model most accurately describes the experiment at hand. However it can be argued that there are still significant residuals remaining, especially in the force signal. The force residuals are highest at the dashed lines, which are exactly at the bottom of the unloading cycles. The followed method of successively enriching the model can be continued to also isolate the constitutive behavior that is causing this residual. However, this is considered beyond the scope of this paper. An obvious candidate for future enrichments would be models that can account for

the observed reduction in elastic modulus like, for instance, damage.

4. Conclusions

The experiment discussed herein is a uniaxial tensile test. The sample geometry was not optimized for identifying anisotropic plasticity. However through the use of full-field identification methods, it was possible to identify 10 parameters from a *single* experiment to varying accuracy. This analysis shows that the data density, which is currently attainable, is very rich and full-field identification methods can benefit from all of them.

Identification is a process to minimize the experiment/simulation gap. In this process, having more degrees of freedom in the material model typically allows for reducing the model error. For cases where the residuals are much greater than the expected uncertainty it is important to evaluate the shape or signature of the residual. Comparing the residual fields to sensitivity fields of perhaps previously unused parameters will highlight if the corresponding model enrichments will have an impact on the identification quality.

For full-field identification methods, tools like residual and sensitivity fields are part of the procedure. Therefore, they are accessible and valuable for gradually improving the identification results. Even for other methods, where these fields are not readily available, it is always possible to obtain them by simulating the experiment and comparing the measured quantities with their simulated counterparts. Similarly, sensitivity fields can be constructed from perturbations of the same simulation. In most cases, the goal of obtaining the material parameters is to use them in FE simulations. Consequently, this proposition is only a small and highly advisable extra step.

Last, enriching the material models gradually reduced the residuals. In particular it was shown that a significant reduction in residuals occurs when full-field data are used instead of the classical way of identifying models with such a simple geometry. Further, as long as the parameters are independent enough, enriching the model not only identifies a more complex material behavior but

also reduces the residual. The previous parameters will be identified to greater accuracy as well.

Acknowledgement

It is a pleasure to acknowledge the support of BPI France within the "DIC-CIT" project.

References

[1] M. F. Ashby and D. R. J. Jones. *Engineering materials 2: an introduction to microstructures, processing and design*, vol. 39. Pergamon Press (1986)

[2] J. Lemaitre and J. L. Chaboche. *Mechanics of Solid Materials*. Cambridge University Press, Cambridge (UK) (1990)

[3] J. Lemaitre, ed. *Handbook of Materials Behavior Models*. Academic Press, San Diego (USA) (2001)

[4] M. A. Sutton, J.-J. Orteu and H. Schreier. *Image Correlation for Shape, Motion and Deformation Measurements*. Springer US, Boston, MA (2009)

[5] M. A. Sutton. *Computer Vision-Based, Noncontacting Deformation Measurements in Mechanics: A Generational Transformation*. Applied Mechanics Reviews, 65(5):1–23 (2013). doi:10.1115/1.4024984

[6] ASTM. *E8 / E8M-15a, Standard Test Methods for Tension Testing of Metallic Materials*, vol. 03.01. ASTM International, West Conshohocken, PA (USA) (2015)

[7] M. Bonnet and A. Constantinescu. *Inverse problems in elasticity*. Inverse Problems, 21(2):R1–R50 (2005)

[8] A. Baldi. *Full field methods and residual stress analysis in orthotropic material. II: Nonlinear approach*. International Journal of Solids and Structures, 44(25-26):8244–8258 (2007). doi:10.1016/j.ijsolstr.2007.06.002

[9] M. Grédiac and F. Hild, eds. *Full-Field Measurements and Identification in Solid Mechanics*. ISTE / Wiley, London (UK) (2012)

[10] K. T. Kavanagh and R. W. Clough. *Finite element applications in the characterization of elastic solids*. International Journal of Solids and Structures, 7:11–23 (1971)

[11] M. H. H. Meuwissen, C. W. J. Oomens, F. P. T. Baaijens, R. Petterson and J. D. Janssen. *Determination of the elasto-plastic properties of aluminium using a mixed numerical–experimental method*. Journal of Materials Processing Technology, 75(1-3):204–211 (1998)

[12] O. Ghouati and J. Gelin. *Identification of material parameters directly from metal forming processes*. Journal of Materials Processing Technology, 80-81:560–564 (1998). doi:10.1016/S0924-0136(98)00159-9

[13] S. Avril, M. Bonnet, A.-S. Bretelle, M. Grédiac, F. Hild, P. Ienny, F. Latourte, D. Lemosse, S. Pagano, E. Pagnacco and F. Pierron. *Overview of Identification Methods of Mechanical Parameters Based on Full-field Measurements*. Experimental Mechanics, 48(4):381–402 (2008)

[14] T. Pottier, F. Toussaint and P. Vacher. *Contribution of heterogeneous strain field measurements and boundary conditions modelling in inverse identification of material parameters*. European Journal of Mechanics, A/Solids, 30(3):373–382 (2011). doi:10.1016/j.euromechsol.2010.10.001

[15] W. Wang, J. E. Mottershead, C. M. Sebastian and E. A. Patterson. *Shape features and finite element model updating from full-field strain data*. International Journal of Solids and Structures, 48(11-12):1644–1657 (2011). doi:10.1016/j.ijsolstr.2011.02.010

[16] S. Roux and F. Hild. *Stress intensity factor measurements from digital image correlation: Post-processing and integrated approaches*. International Journal of Fracture, 140(1-4):141–157 (2006). doi:10.1007/s10704-006-6631-2

[17] H. Leclerc, J.-N. Périé, S. Roux and F. Hild. *Integrated digital image correlation for the identification of mechanical properties.* In A. Gagalowicz and W. Philips, eds., *Mirage2009*, pp. 161–171. Springer, Berlin Heidelberg (2009)

[18] J. Réthoré. *A fully integrated noise robust strategy for the identification of constitutive laws from digital images.* International Journal for Numerical Methods in Engineering, 84:631–660 (2010)

[19] J. Réthoré, Muhibullah, T. Elguedj, M. Coret, P. Chaudet and A. Combescure. *Robust identification of elasto-plastic constitutive law parameters from digital images using 3D kinematics.* International Journal of Solids and Structures, 50(1):73–85 (2013)

[20] F. Mathieu, H. Leclerc, F. Hild and S. Roux. *Estimation of Elastoplastic Parameters via Weighted FEMU and Integrated-DIC.* Experimental Mechanics (2014). doi:10.1007/s11340-014-9888-9

[21] J. Neggers, J. P. M. Hoefnagels, M. G. D. Geers, F. Hild and S. Roux. *Time-Resolved Integrated Digital Image Correlation.* International Journal for Numerical Methods in Engineering, 103:157–182 (2015). doi:10.1002/nme.4882

[22] A. Tarantola and B. Valette. *Inverse Problems = Quest for Information.* Journal of Geophysics, 50(3):159–170 (1982). doi:10.1038/nrn1011

[23] S. Cooreman, D. Lecompte, H. Sol, J. Vantomme and D. Debruyne. *Elasto-plastic material parameter identification by inverse methods: Calculation of the sensitivity matrix.* Int. J. Solids Struct., 44(13):4329–4341 (2007)

[24] E. Pagnacco, A. S. Caro-Bretelle and P. Ienny. *Parameter Identification from Mechanical Field Measurements using Finite Element Model Updating Strategies*, pp. 247–274. ISTE / Wiley, London (UK) (2012)

[25] D. Claire, F. Hild and S. Roux. *A finite element formulation to identify damage fields: the equilibrium gap method.* International Journal for Numerical Methods in Engineering, 61(2):189–208 (2004)

[26] M. Grédiac and F. Pierron. *Applying the Virtual Fields Method to the identification of elasto-plastic constitutive parameters.* International Journal of Plasticity, 22(4):602–627 (2006). doi:10.1016/j.ijplas.2005.04.007

[27] S. Avril, F. Pierron, M. A. Sutton and J. Yan. *Identification of elasto-visco-plastic parameters and characterization of Lüders behavior using digital image correlation and the virtual fields method.* Mechanics of Materials, 40(9):729–742 (2008). doi:10.1016/j.mechmat.2008.03.007

[28] F. Hild and S. Roux. *Digital Image Correlation: from Displacement Measurement to Identification of Elastic Properties - a Review.* Strain, 42(2):69–80 (2006)

[29] D. Lindner, F. Mathieu, F. Hild, O. Allix, C. Ha Minh and O. Paulien-Camy. *On the evaluation of stress triaxiality fields in a notched titanium alloy sample via integrated {DIC}.* J. Appl. Mech., 82(7):71014 (2015). doi:10.1115/1.4030457

[30] F. Hild and S. Roux. *Comparison of Local and Global Approaches to Digital Image Correlation.* Experimental Mechanics, 52(9):1503–1519 (2012)

[31] A. P. Ruybalid, J. P. M. Hoefnagels, O. van der Sluis and M. G. D. Geers. *Comparison of the identification performance of conventional FEM updating and integrated DIC Andre.* International Journal for Numerical Methods in Engineering, 106:298–320 (2016)

[32] M. Rossi and F. Pierron. *On the use of simulated experiments in designing tests for material characterization from full-field measurements.* International Journal of Solids and Structures, 49(3-4):420–435 (2012). doi:10.1016/j.ijsolstr.2011.09.025

[33] M. B. R. Bertin, F. Hild and S. Roux. *Optimization of a cruciform specimen geometry for the identification of constitutive parameters based upon full-field measurements.* Strain, 52(4):307–323 (2016). doi:10.1111/str.12178

[34] A. N. Tikhonov and V. Y. Arsenin. *Solutions of ill-posed problems.* J. Wiley, New York (USA) (1977)

[35] R. Gras, H. Leclerc, F. Hild, S. Roux and J. Schneider. *Identification of a set of macroscopic elastic parameters in a 3D woven composite: Uncertainty analysis and regularization.* International Journal of Solids and Structures (2014). doi:10.1016/j.ijsolstr.2013.12.023

[36] H. Leclerc, J. Neggers, F. Mathieu, F. Hild and S. Roux. *Correli* (2016). doi:IDDN.FR.001.520008.000.S.P.2015.000.31500

[37] Dassault Systèmes Simulia. *Abaqus Analysis User's Manual*, vol. 3 Material. Dassault Systèmes Simulia (2012)

[38] D. Banabic, H.-J. Bunge, K. Pöhlandt and A. E. Tekkaya. *Formability of metallic materials.* Springer (2000). doi:10.1007/978-3-662-04013-3

[39] H. Kleemola and M. Nieminen. *On the strain-hardening parameters of metals.* Metallurgical Transactions, 5:1863–1866 (1974)

[40] R. Hill. *A theory of the yielding and plastic flow of anisotropic metals.* Proc. Roy. Soc. London, 193:281–297 (1948)